minerals

MDPI

Article

Pore Structure and Fractal Dimension Analysis of Nephrite Deposits in Luanchuan, Western Henan, Central China

Xiaodi Wang [1,2], Weiqing Liu [1,*], Lixin Zhang [2], Wei Wu [1], Qing Ma [2] and Junwei Song [2]

[1] School of Resources and Environment, Henan Polytechnic University, Jiaozuo 454003, China; wangxiaodi202506@163.com (X.W.); wei@hpu.edu.cn (W.W.)
[2] Henan Institute of Product Quality Inspection Technology, Zhengzhou 450047, China; 13598859582@163.com (L.Z.); ma_qing2007@163.com (Q.M.); 19069633777@163.com (J.S.)
* Correspondence: liuweiqing1212@126.com

Abstract

Pore structure and fractal dimension analysis of nephrite deposits are essential for assessing potential quality, conducting investigations, and exploiting jade resources. This research explored nephrite (tremolite) jade from Tonggou in the Luanchuan Group, utilizing techniques such as scanning electron microscopy (SEM), X-ray diffraction (XRD), and low-temperature nitrogen adsorption (LT-N_2GA) to illustrate the pore structure of the jade deposit and to examine its developmental features, complexity, and implications for jade quality assessment. The findings revealed that the Tonggou nephrite jade deposit comprises three varieties of micropores. The nitrogen adsorption curve was similar to type IV, featuring hysteresis loops that were mainly classified as H_2 and H_3, suggesting a predominantly mesoporous nature. The fractal dimensions (D_{F1} and D_{F2}), determined using the FHH model, averaged 2.474 and 2.572, respectively. This implies that the pore surface of the Tonggou jade deposit is irregular, the pore structure is intricate, and displays a pronounced heterogeneity. In the Tonggou deposit, the specific surface area (SSA) and pore volume (PV) show moderate positive and negative correlations with antigorite and calcite, respectively. Tremolite exhibits a strong negative correlation with SSA. The fractal dimension reveals weak, moderate, and strong negative correlations with SSA, PV, and average pore size (APS), respectively. As the content of siliceous minerals increases, the fractal dimension gradually increases. Conversely, a rise in carbonate mineral content results in a gradual decrease in the fractal dimension.

Keywords: pore structure; nephrite deposit; West Henan; fractal dimension; LT-N_2

1. Introduction

The history of jade culture is extensive, with nephrite being its most distinguished variety. Nephrite (tremolite) jade is valued for its unique creamy color and oily luster, and its durability has made it a beloved choice among consumers in China and internationally [1,2]. Nephrite jade is typically made up of fibrous amphibole minerals, such as tremolite and actinolite, with the chemical formula of $Ca_2(Mg,Fe)_5Si_8O_{22}(OH)_2$. It commonly appears in colors ranging from light to dark green, yellow to brown, white, gray, and black. The premium "sheep suet" white jade often has a composition similar to that of tremolite [3,4].

Nephrite deposits are distributed worldwide and have two main kinds: skarn-associated deposits related to contact metamorphism and serpentine-associated deposits related to mantle subduction [5]. Nephrite deposits are scarce, but occur in many regions around the world.

Check for updates

Received: 8 January 2026
Revised: 29 January 2026
Accepted: 30 January 2026
Published: 3 February 2026

The marble-type nephrite is found in many areas in China, Korea, and South Australia [6–8]. The other type is known from Canada, New Zealand, Russia, and Taiwan [9,10]. A large number of studies have shown that the majority of nephrite jade deposits worldwide are situated within ophiolite, where the mineral forms via Ca- and Si-rich aqueous fluid-mediated metasomatic replacement under low-grade metamorphic conditions or lower P-T conditions [11].

Most studies thus far have concentrated on petrological, mineralogical characteristics and age dating [12–15], with systematic studies on pore structure and fractal trait of nephrite jade linked to serpentinite bodies being less common, particularly in the investigation of pore space heterogeneity [16,17]. Nephrite from different origins exhibits varying characteristics of porosity. Comprehending the porosity and fractal dimensions of nephrite is advantageous for assessing the quality of this valuable resource. Consequently, the investigation of the porosity in nephrite jade has become crucial for maintaining quality standards.

The nephrite jade deposit was discovered at the Tonggou serpentine jade open mine in the Qinling orogenic belt, where the sample for this paper was obtained. Commonly associated with the Yi River source, the jade in this region is known commercially as "Yiyuan jade". However, there is no detailed analysis of the deposits, and discussion is ongoing about their pores and fractures.

This paper uses argon-ion polishing SEM for qualitative pore structure and LT-N_2 testing for quantitative pore structure parameters. The relationship between fractal dimensions, mineral composition, and pore structure parameters is summarized based on the fractal dimension variation rule of micro-pore structure obtained from the fractal hierarchical model (FHH). The significant influence of fractal dimension on the adsorption of nephrite deposit is emphasized. This gives a scientific basis and data for nephrite jade assessment in West Henan, Central China. In this paper, we propose a new approach for the qualitative analysis, pore structure analysis, and fracture analysis of nephrite deposits.

2. Geological Settings and Methods

2.1. Geological Settings and Samples

The Tonggou jade deposit is located in the Qinling orogenic belt, known for its significant geological tectonic activity [18,19]. The region has experienced numerous continental collisions, leading to the development of faults and folds that have caused both brittle and ductile deformation in the rock formations within the mining site [20–22]. The samples of this research were collected from two open-pit jade mines in Tonggou, approximately 21 km northwest of Luanchuan, Henan Province, Central China. The geographical coordinates of the jade deposit range from a longitude of 111°23′54″ E to 111°24′16″ E, and a latitude of 33°53′40″ N to 33°54′08″ N (Figure 1). The lithologies of the ore bodies have all primarily undergone strong serpentinization (Figure 2). Although nephrite and serpentine jade are closely related, their chemical compositions are $Ca_2(Mg,Fe)_5Si_8O_{22}(OH)_2$ and $(Mg,Fe,Ni)_3Si_2O_5(OH)_4$, respectively, with Mohs hardness ranging from 6.0–6.5 to 2.5–6.0. The white and green jade have higher market value, both possessing unique characteristics.

The nephrite hand specimens display two distinct colors: white and light grayish–white (Figure 3a,d). The high-value white "sheep suet" jade has not been mined in this study area. Tonggou jade is fine-grained, and most of the finished jade products exhibit a semi-transparent state and an oily luster. The serpentine in the Tonggou jade mine is primarily green and yellow–green, and most of the finished jade products possess a glassy luster (Figure 3b,c,e,f). The jade products processed by the Tonggou jade mine are marketed as "Yiyuan jade," and items such as "Yiyuan jade" shan-shaped ornaments, landscape decorative paintings, Avalokiteshvara, and Buddha pendants are favored by many Chinese consumers while serving as popular cultural souvenirs for tourists (Figure 3g,h,i).

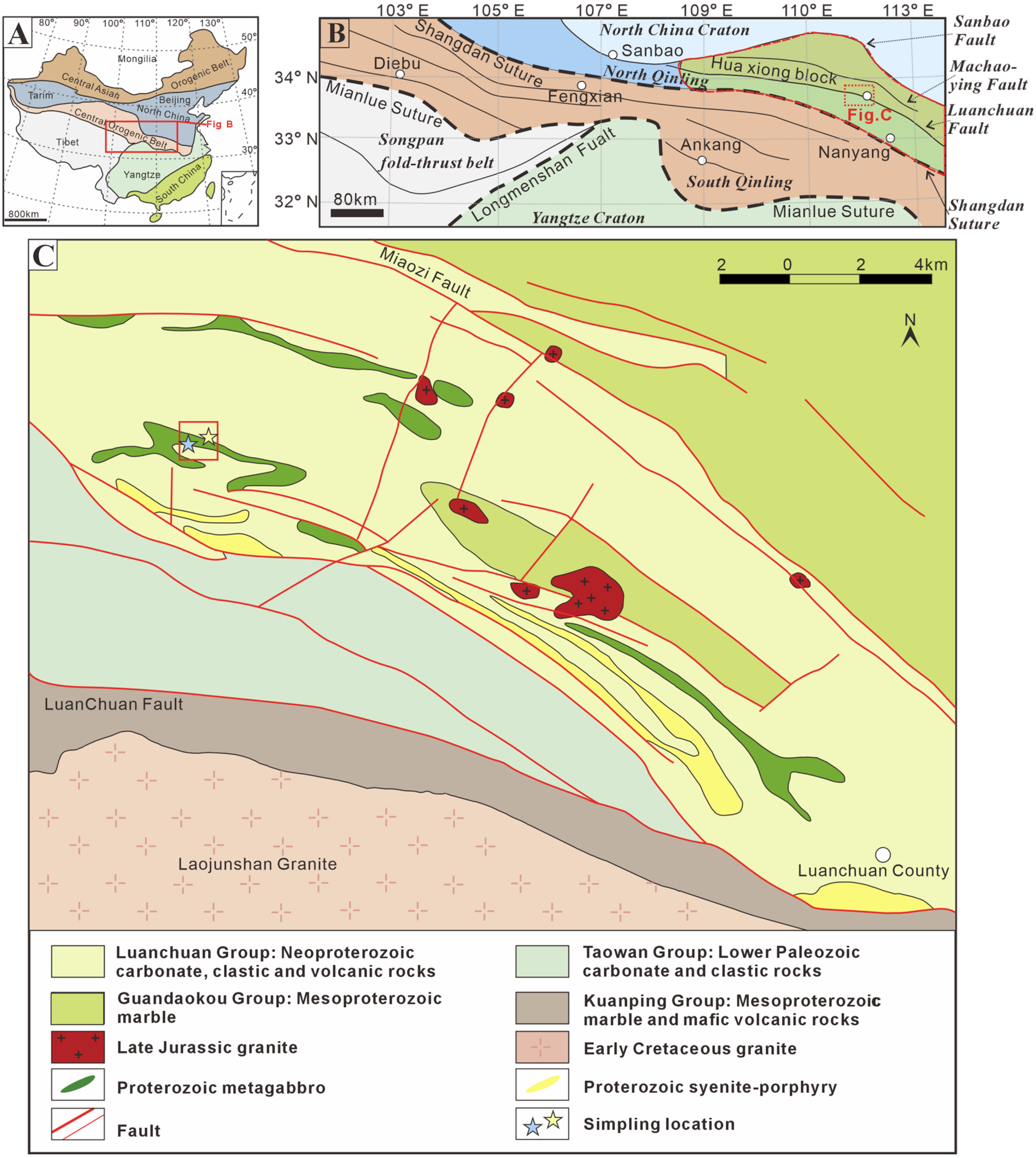

Figure 1. (**A**) Tectonic map of China; (**B**) division of Qinling Orogen with Luanchuan district; (**C**) Luanchuan Tonggou jade deposit in the area. (Modified from Mao et al. (2011a), Li et al. (2012a), Yang et al. (2013) [23–25]).

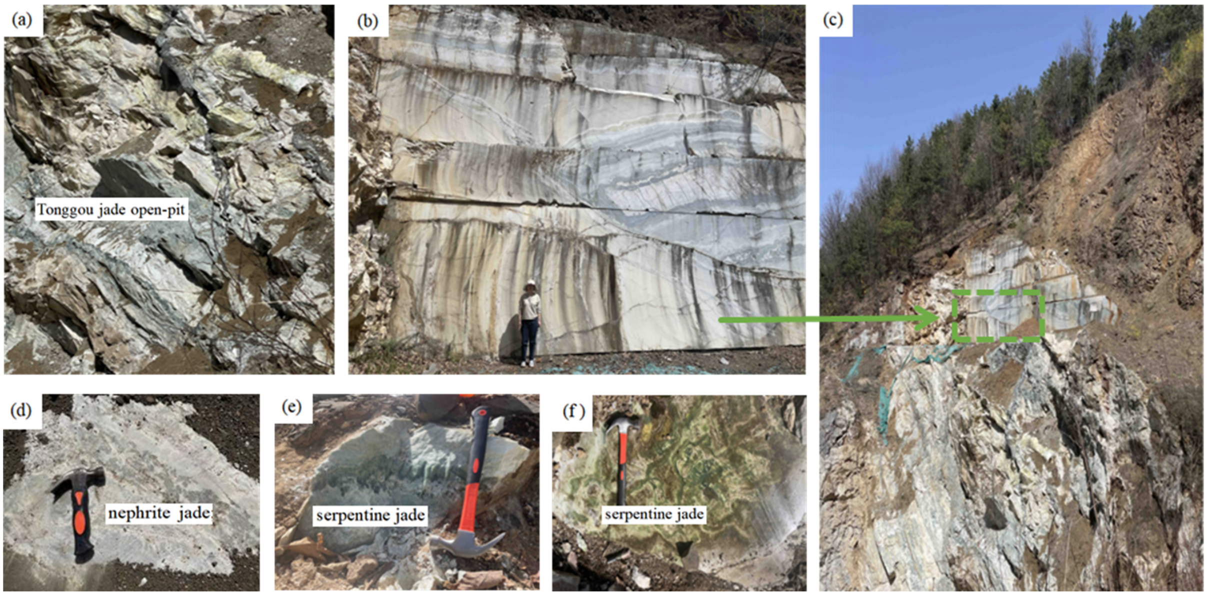

Figure 2. (**a**) Tonggou open-pit serpentine rocks; (**b**) top view of the jade mine (featuring author Xiaodi Wang); (**c**) Tonggou jade open-pit (picture (**b**) was taken at the green border of picture (**c**)); (**d**) grayish–white nephrite jade vein; (**e**) green serpentine jade rough; (**f**) high-quality yellowish–green serpentine jade rough.

Figure 3. Examples of jade specimens, processed products and ornaments: (**a**) grayish–white nephrite specimen; (**b**) serpentine jade mixed yellow and white; (**c**) serpentine jade mixed yellow and green;

(**d**) white nephrite bracelet; (**e**) deep green serpentine jade specimen; (**f**) green serpentine jade transparent to transmitted light; (**g**) Yiyuan jade shan ornament; (**h**) Yiyuan jade landscape decorative painting; (**i**) Yiyuan jade Avalokiteshvara and Buddha pendants symbolizing peace and health. (photos (**g**–**i**) were taken by author Xiaodi Wang, showing jade products and ornaments for sale at a Yiyuan jade store); Tr: tremolite; Srp: serpentine.

The pore system between the green-to-yellowish–green serpentine and white-to-pale-grayish–white nephrite in the study area affects quality evaluation factors such as transparency, toughness, brittleness, and later development and use of jade economic resources. The economic value of processed Tonggou jade products, such as Yiyuan jade Mountain model ornaments, depends on the degree of micro-crack development. Micro-cracks on the surface of jade items decrease their value. During mining, selection, and processing processes, the pore structure and micro-fracture development must be considered. Therefore, the work presented here is important.

2.2. Experimental Methods

A total of 15 samples with typical texture characteristics from the Tonggou jade mine encompass jade vein characteristic samples (YMT1–4, YMS1–4), contact zone characteristic samples (JC1–5), and surrounding rock unit characteristic samples (WY1–2). The pore structure of these samples was successively tested using SEM, XRD, and LT-N_2GA, and their fractal characteristics were identified using the FHH model (Table 1).

Table 1. Experimental methods for samples.

Experimental Method	Instrument Model	Sample Specifications	Experimental Conditions
XRD	Rigaku SmartLab	300 mesh powder with a weight of 1–2 g	Cu target, 5° to 70°, 10°/min
SEM	GeminiSEM 360	1.0 cm × 1.0 cm × 0.5 cm cubic	15 kV, 19 °C, 65%
LT-N2	MicrotracBEL BELSORPMINI X	200 mesh powder with a weight of 2–3 g	77.3 K

A sample was ground into a standard 300-mesh uniform powder, and its component content was tested using the Rigaku SmartLab (Rigaku Corporation, Tokyo, Japan) X-ray instrument at the Zhengzhou Laboratory in China. Based on the sample's characteristics, the test was conducted in accordance with the experimental requirements for a Cu target, scanning from 5 degrees to 70 degrees at a rate of 10 degrees per minute.

Specimens from the Tonggou jade mine were carefully crafted into cubic thin slices with dimensions of 1.0 cm × 1.0 cm × 0.5 cm. Utilizing state-of-the-art GeminiSEM 360 (Carl Zeiss, Oberkochen, Germany), the pore-fracture architecture was scrutinized. This analysis took place within the controlled parameters of the Zhengzhou Laboratory in China, with a voltage of 15 kV, ambient temperature of 19 °C, and relative humidity set at 65%.

The LT-N_2 experimental test necessitates the sample to be ground to 200 mesh and vacuum-dried prior to testing to enhance accuracy. The characteristic samples from the Tonggou jade mine were tested using the MicrotracBEL BELSORPMINI X (Microtrac, Newtown, PA, USA) instrument at the Zhengzhou Laboratory in China for high-purity nitrogen adsorption experiments. Adsorption–desorption isotherms were obtained at a temperature of 77.3 K, and PV, SSA, and PSD data were calculated using the Barrett-Joyner-Halenda (BJH) method.

This study utilized the taxonomic characteristics of minerals and employed the FHH model for data analysis [26]. The fractal dimensions D_{F1} and D_{F2} correspond to the medium–low-pressure and high-pressure data of the Tonggou jade deposit, respectively.

$$\mathrm{In}(V) = (D_F - 3) \times \mathrm{In}(\mathrm{In}(\frac{P_0}{P})) + c \quad (1)$$

In Formula (1), P, P_0, and V represent the equilibrium pressure (MPa), saturated vapor pressure (MPa), and gas adsorption volume (cm^3/g) at equilibrium pressure P, respectively.

3. Results

3.1. Mineral Components

The species and content of minerals extracted from jade deposits can reflect the various types of geological tectonic movements and redox environments that the deposits have undergone. This has a significant impact on the subsequent evaluation of economic value and quality of jade, as well as on the assessment of mining potential.

The Jade ver. 9.0 software was employed to analyze jade phases corresponding to each diffraction peak. The crystal structures of these phases were retrieved from the crystallographic database. Using the full-peak-fit (WPF) method combined with Rietveld refinement, the relative content of each phase was determined. The quantitative analysis was based on the Rietveld method, with an estimated error margin of approximately 5% for the final proportions. No significant preferred orientation was observed. The main minerals and PDF numbers are as follows: antigorite (PDF#00-007-0417), lizardite (PDF#00-050-1625), tremolite (PDF#00-044-1402), calcite (PDF#01-072-4582), dolomite (PDF#01-081-8227), chlorite (PDF#00-007-0078), brucite (PDF#01-071-5972), diopside (PDF#01-073-6374), hematite (PDF#01-071-5088), wüstite (PDF#01-074-1886) and quartz (PDF#01-070-7344).

XRD analysis revealed that jade veins in the Tonggou nephrite deposit predominantly consist of antigorite, lizardite, tremolite, calcite, dolomite, and chlorite. The contact zones contain serpentine-group minerals, carbonates, clay minerals, brucite, diopside, hematite, and wüstite, whereas the wall rocks are characterized by serpentine, carbonates, quartz, and chlorite (Table 2; Figure 4). Antigorite and lizardite are polytypic varieties within the phyllosilicate serpentine $(Mg,Fe,Ni)_3Si_2O_5(OH)_4$ group. Lizardite, characterized by a platy structure, is stable under low-temperature conditions, whereas antigorite, distinguished by its characteristic wavy or corrugated structure, forms under relatively high-temperature and high-pressure environments. The presence and abundance of antigorite in the Tonggou jade deposit indicate that the orebody has undergone regional metamorphism involving elevated temperature and pressure. This metamorphic history is consistent with the formation conditions of tremolite, a double-chain silicate belonging to the amphibole group.

Four key mineral assemblages were identified: silicate phases dominated by tri-octahedral serpentine content ranging from 50.9% to 93.1%, 2D layered structures and double-chain tremolite content between 3.1% and 99.3%, carbonate phases comprising calcite (18.6–72.1%) and dolomite (1.9–24.6%), and clay minerals represented by trioctahedral 2:1-type chlorite content ranging from 2.9 to 8.5% (Figure 5). The presence of hematite and wüstite indicates the redox conditions of the jade deposit. Therefore, the Tonggou jade deposit in the study area exhibits growth characteristics of high-silica minerals and low-clay minerals.

Table 2. Mineral assemblages of the investigated samples.

Samples	Lithology	Mohs Hardness	Main Mineral Assemblages
YMT-1	Grayish–white jade	2.5–6.5	Cal, Atg, Lz, Dol, Tr
YMT-2	Light grayish–white jade	2.5–6.5	Cal, Tr, Atg, Chl
YMT-3	Grayish–white jade with brownish–yellow stains	3.0–6.5	Tr, Cal
YMT-4	Grayish–white jade	3.0–6.5	Tr, Cal
YMS-1	White-to-green jade	2.5–6.0	Atg, Cal, Lz, Dol
YMS-2	Grayish–white-to-green jade	2.5–6.0	Atg, Cal, Dol
YMS-3	Deep green jade	2.5–6.0	Atg, Lz
YMS-4	Yellow-to-green jade	2.5–6.0	Atg, Lz, Cal, Dol
JC-1	Yellow-to-white jade	2.0–6.0	Cal, Dol, Atg, Brc, Lz, Chl
JC-2	Green jade	2.5–6.5	Di, Cal, Atg, Chl, Lz, Hm
JC-3	Yellow-to-green jade	2.5–6.0	Atg, Dol, Lz, Wu, Cal
JC-4	Green jade	2.5–6.0	Atg, Cal, Chl, Di, Lz
JC-5	Light green jade	2.5–6.0	Atg, Cal, Lz, Dol
WY-1	Light yellow-to-green jade	2.5–6.5	Cal, Atg, Dol, Qz
WY-2	Grayish–white jade	2.5–6.5	Cal, Brc, Dol, Chl, Atg, Qz

Dol, dolomite; Cal, calcite; Brc, brucite; Chl, clinochlore; Lz, lizardite; Atg, antigorite; Di, diopside; Hm, hematite; Tr, tremolite; Wu, wüstite; Qz, quartz.

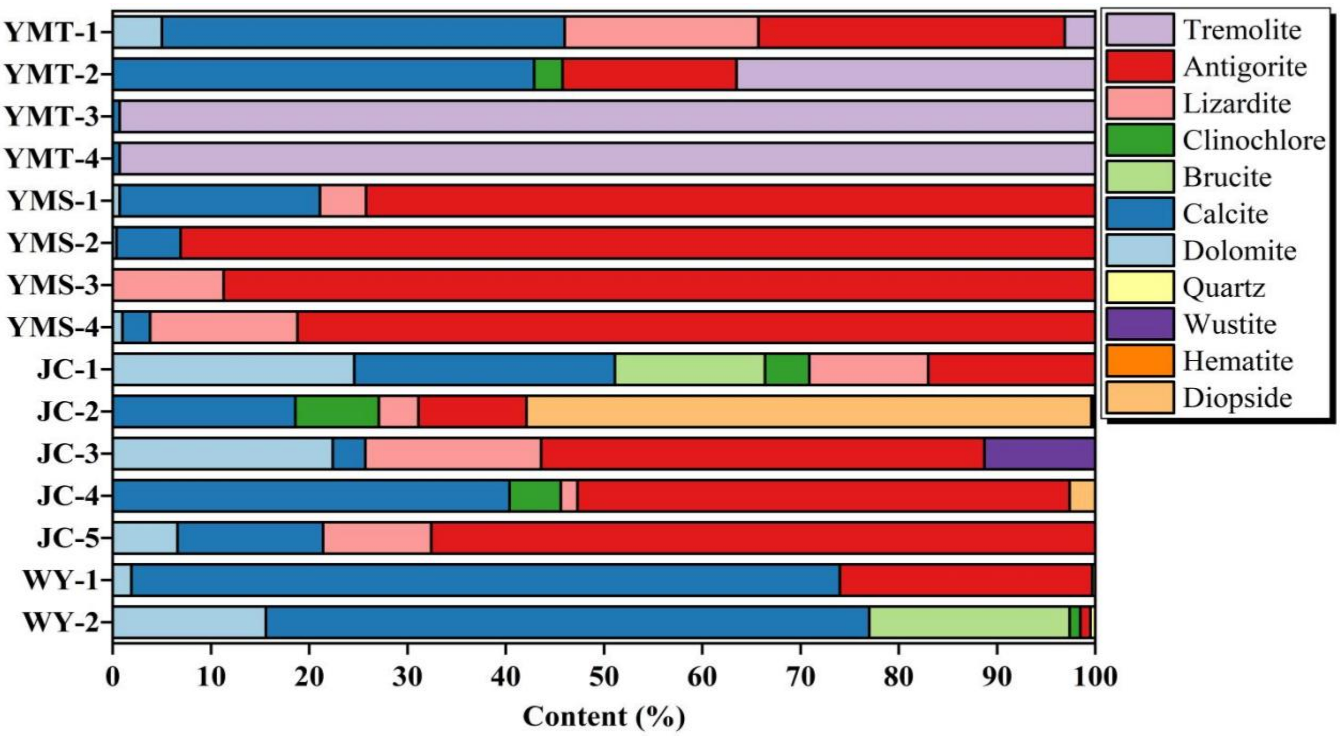

Figure 4. The bar graph for the studied samples.

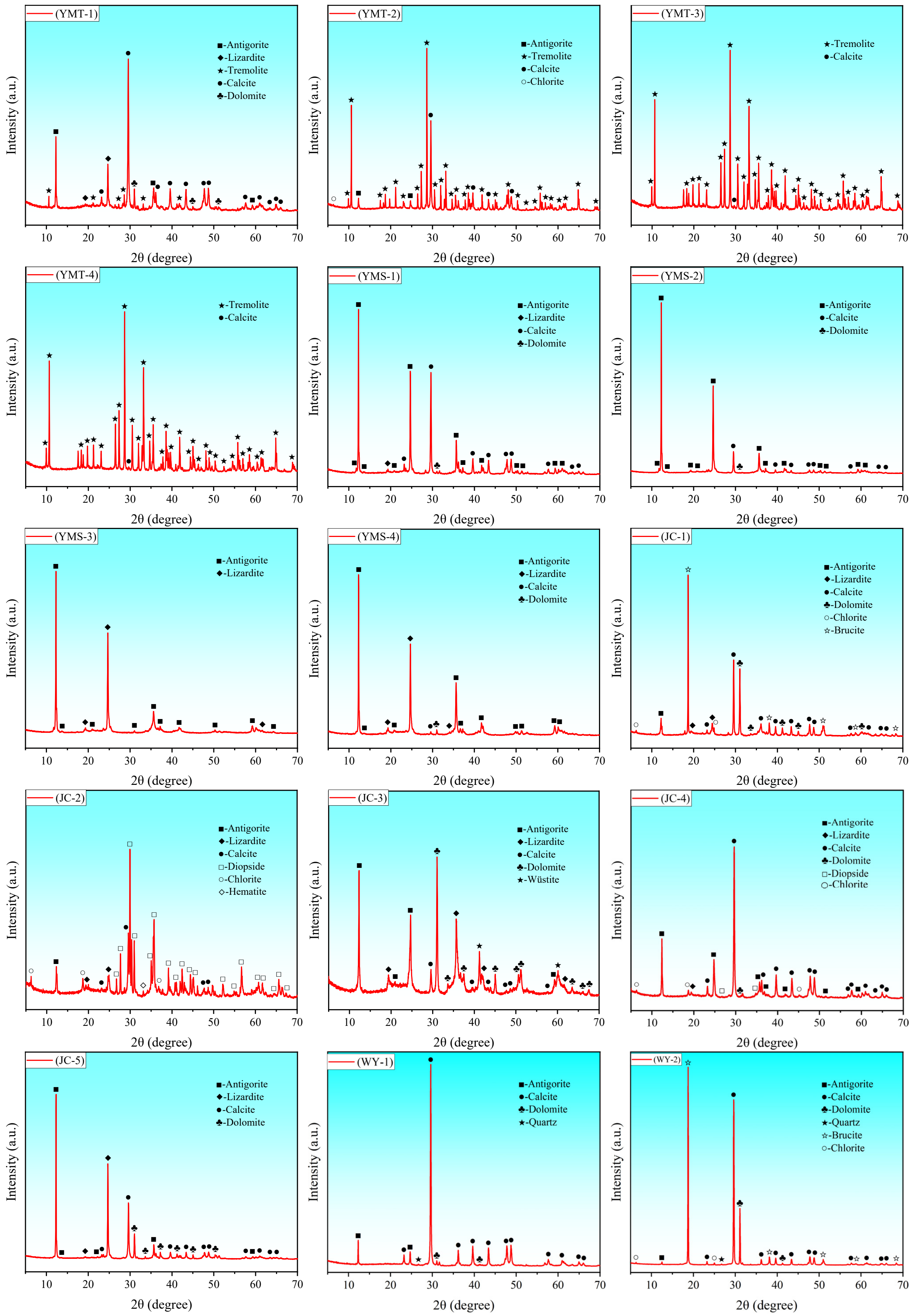

Figure 5. Mineral composition of the samples.

3.2. Pore Surface Morphology

Numerous geologists have studied pore–fracture structures. According to the type, distribution, size, and connectivity of the pores, the microstructure of the Tonggou jade deposit is divided into intragranular pores, intergranular pores, and microfractures [27]. Microfractures are prominently present in jade veins, contact areas, and surrounding rocks, suggesting a complex and vigorous fold-and-fault activity [28,29].

The silicate minerals antigorite and lizardite, with typical layers in jade veins, exhibit both intragranular and intergranular pores. These pores are connected in series and provide large-scale pores. After extensive diagenesis and jade formation, different kinds of intergranular pores, such as needle-like, strip-like, and slit-like pores, occur along grain boundaries of different mineral types due to differing hardness and grain structure (Figure 6). Carbonate minerals (calcite and dolomite) in the Tonggou jade deposit undergo dissolution after metamorphication leading to small pores [30].

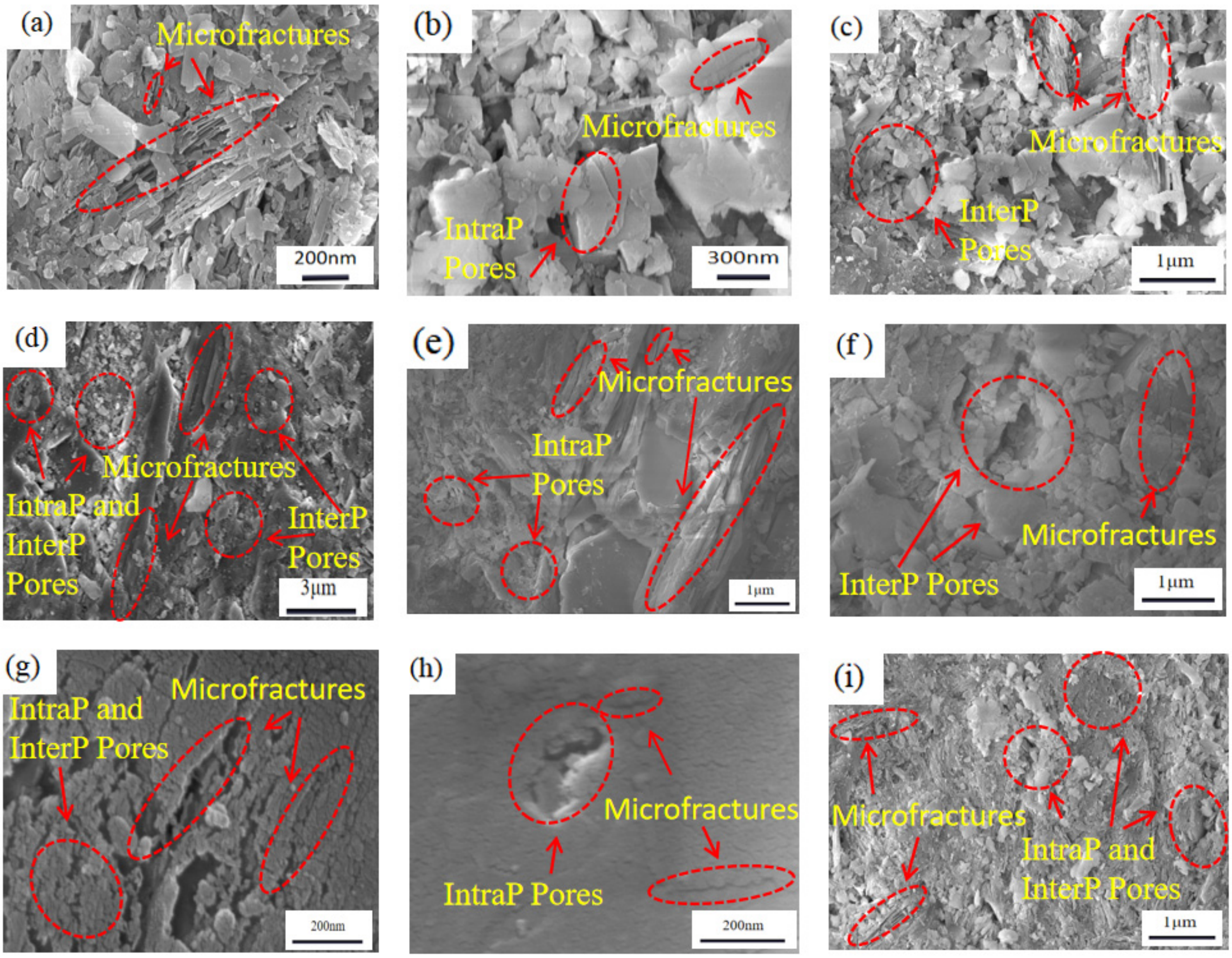

Figure 6. (**a**) Microfractures in sample YMS-2; (**b**,**c**) microfractures, interP pores, and intraP pores in sample YMT-1; (**d**–**f**) pore system and microfractures in sample YMS-4; (**g**) serpentine and microfracture lines in sample WY-1; (**h**,**i**) pore system and microfractures in sample JC-2. The red circles indicate the key signal regions.

3.3. Pore Characteristics via LT-N_2 Adsorption

The nitrogen isotherms of 15 samples from the Tonggou jade deposit are of type IV, as shown by H_2 and H_3 of the IUPAC scheme. In the typical jade vein sample (YMS-4) and the surrounding rock sample (WY1–2) of the Tonggou jade deposit, we observe a sharp hysteresis loop as P/P_0 approaches 0.5, and the shape of this loop resembles the H2 model. The test analysis diagrams of jade vein samples (YMT1–4, YMS1–3) and contact zone samples (JC1–5) show a weak sharp point near P/P_0 close to 0.5 (which indicates needle-like and slit-like pore structures), similar to the H_3 scheme for adsorption curve categorisation standard (Figure 7).

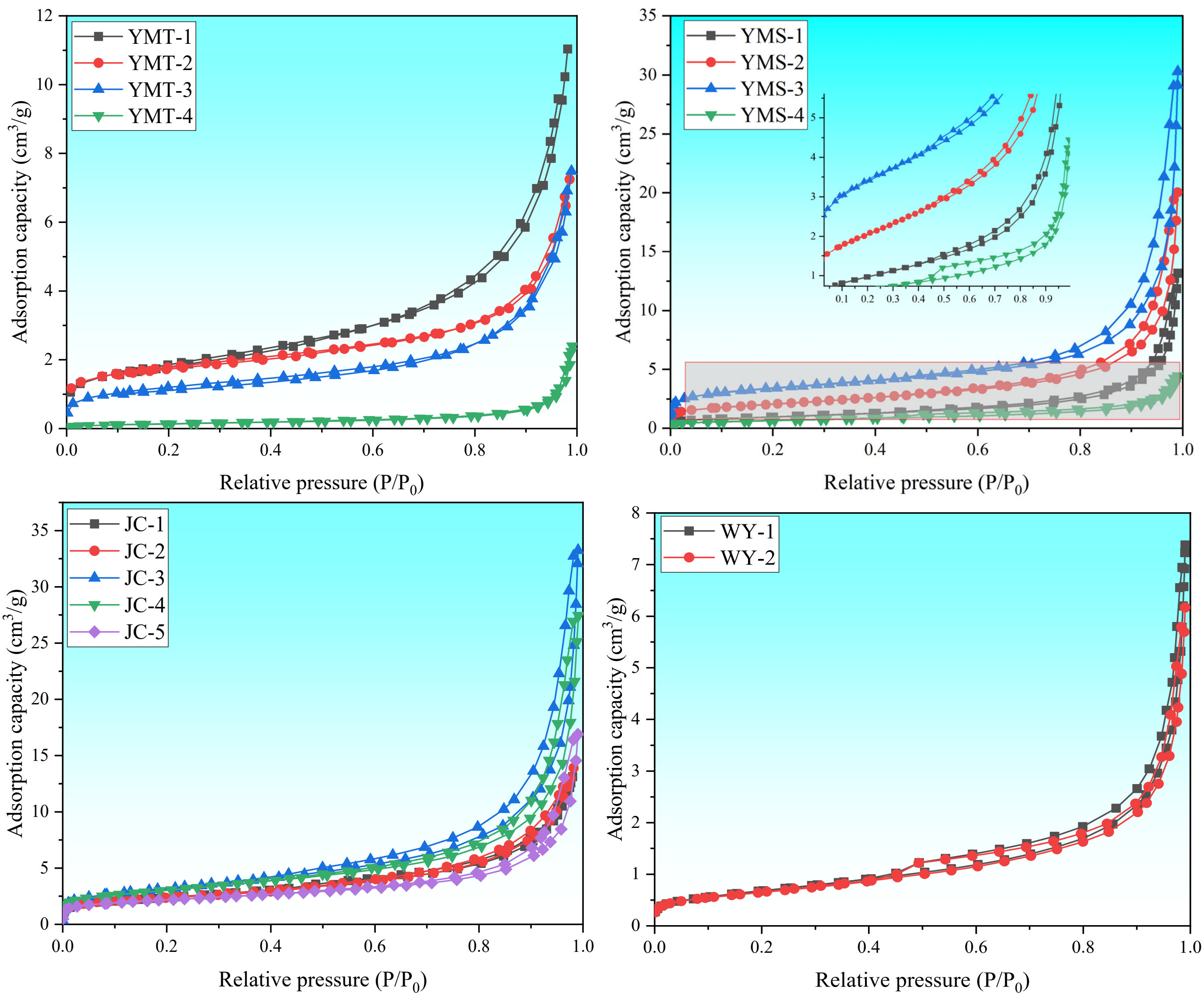

Figure 7. LT-N_2 adsorption curve. Insets show a magnified view of the gray region for clarity.

PSD properties of samples from the Tonggou jade deposit were analyzed using the BJH theory. Pore size distributions in jade vein, contact zone, and wall rock regions ranged from 9.566 to 19.336 nm with an average value of 12.867 nm. The samples exhibited a range of total PV from 0.0036 to 0.0496 cm^3/g and total SSA from 2.823 to 14.136 m^2/g. The average values for PV and SSA were 0.0204 cm^3/g and 6.431 m^2/g, respectively (Table 3).

The particle size distribution (PSD) curves of samples in the study area show that most of the high peak ranges from 3 to 5 nm, and most pores are mesopores. Longitudinally, the YMT-4 jade vein sample has the lowest peak value, while the contact zone sample is the highest. Transversely, the jade vein sample (YMT-4), contact zone sample (JC-1, JC-3), and surrounding rock sample (WY1–2) exhibit a single peak, while other Tonggou jade ore samples exhibit a double-peak pattern between 2–3 nm and 3–5 nm. The pore size distribution curves of jade vein samples (YMS-3, YMS-4) and contact zone samples (JC-3, JC-4) are of 20–65 nm, indicating a high proportion of large pores (Figure 8). A unimodal distribution is indicative of the thorough reworking and homogenization of the original pore architecture due to high-temperature hydrothermal activity. In contrast, a bimodal distribution reveals the superposition of pores formed during multiple geological stages.

Table 3. Data on nitrogen adsorption.

Sample ID	PV (10^{-3} cm^3/g)	SSA (m^2/g)	APS (nm)	FHH					
				$P/P_0 < 0.5$			$P/P_0 > 0.5$		
				K_1	D_{F1}	r_{F1}	K_2	D_{F2}	r_{F2}
YMT-1	14.086	5.292	10.647	−0.450	2.550	−0.9955	−0.402	2.598	−0.9985
YMT-2	7.826	3.223	9.711	−0.331	2.669	−0.9925	−0.308	2.692	−0.9985
YMT-3	10.335	2.949	14.017	−0.416	2.584	−0.9925	−0.390	2.610	−0.9975
YMT-4	3.600	0.737	19.336	−0.728	2.272	−0.9879	−0.569	2.431	−0.9980
YMS-1	19.500	4.377	17.832	−0.580	2.420	−0.9839	−0.513	2.487	−0.9990
YMS-2	29.800	8.939	13.338	−0.676	2.324	−0.9263	−0.451	2.549	−0.9990
YMS-3	43.300	13.415	12.906	−0.612	2.388	−0.8972	−0.456	2.544	−0.9970
YMS-4	6.800	2.823	9.566	−0.540	2.460	−0.9905	−0.358	2.642	−0.9990
JC-1	17.271	6.861	10.069	−0.487	2.513	−0.9869	−0.384	2.616	−0.9990
JC-2	17.954	6.593	10.892	−0.439	2.561	−0.9910	−0.401	2.599	−0.9980
JC-3	49.600	14.136	14.049	−0.582	2.418	−0.9752	−0.460	2.540	−0.9995
JC-4	40.100	12.125	13.234	−0.485	2.515	−0.9823	−0.431	2.569	−0.9995
JC-5	24.900	8.743	11.374	−0.431	2.569	−0.9859	−0.412	2.588	−0.9985
WY-1	11.100	3.213	13.766	−0.576	2.424	−0.9950	−0.460	2.540	−0.9990
WY-2	9.300	3.038	12.273	−0.562	2.438	−0.9925	−0.421	2.579	−0.9995

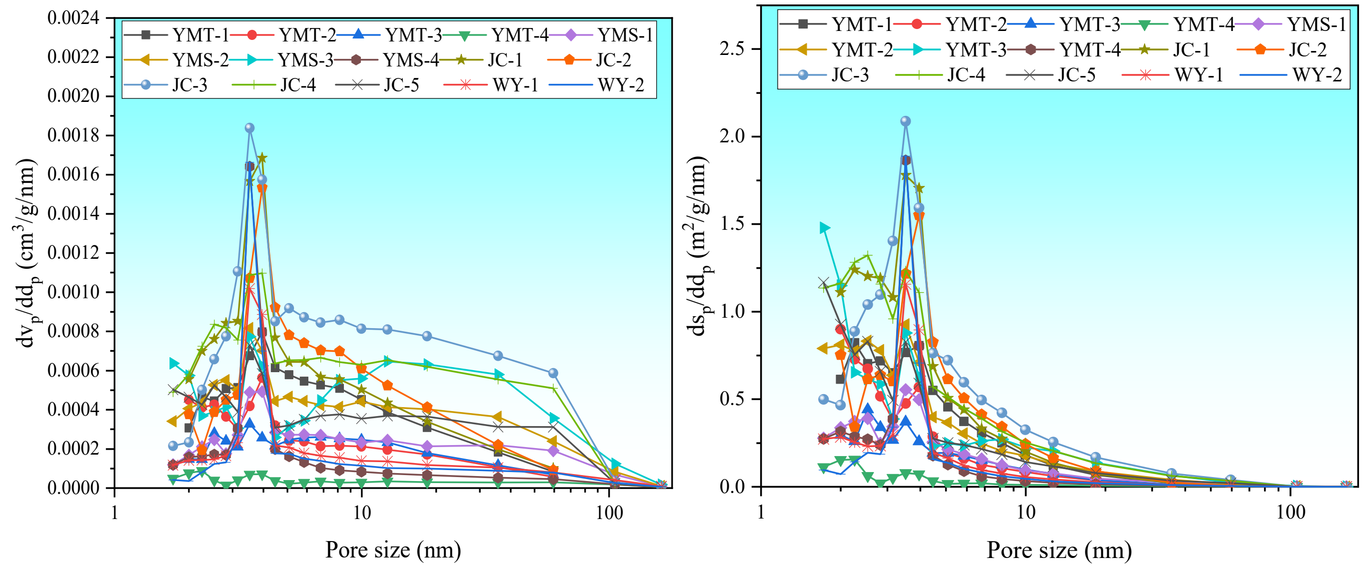

Figure 8. PSD of the jade samples.

3.4. Fractal Characteristics

The fractal data for the Tonggou jade deposit were calculated using Equation (1), derived from the FHH model [31,32]. Within the range of P/P_0 less than 0.5, K_1 and D_{F1} were obtained. All samples exhibited negative K_1 values ranging from −0.728 to −0.331. The highest D_{F1} value was 2.669, with a correlation fitting data r_{F1} of 0.9925, obtained from the jade vein sample (YMT-2). The lowest D_{F1} value was 2.272, with a correlation fitting data r_{F1} of 0.9879, obtained from the jade vein sample (YMT-4).

Within the range of P/P_0 greater than 0.5, K_2 and D_{F2} were obtained. All samples also exhibited negative K_2 values ranging from −0.569 to −0.308. The highest D_{F2} value was

2.692, with a correlation fitting data r_{F2} of 0.9985. The lowest D_{F2} value was 2.431, with a correlation fitting data r_{F2} of 0.9980. The linear fitting data of D_{F2} exhibited high precision, with the average r_{F2} of the Tonggou jade deposit samples exceeding 0.9986 (Table 3).

The higher linear fitting data indicate that the fractal characteristics of the collected samples from the Tonggou jade deposit are more pronounced, with increased heterogeneity and significantly enhanced complexity in the pore structure. The D_{F2} data of the Tonggou jade deposit are higher than the D_{F1} data, but there is no clear regular relationship between them (Figure 9).

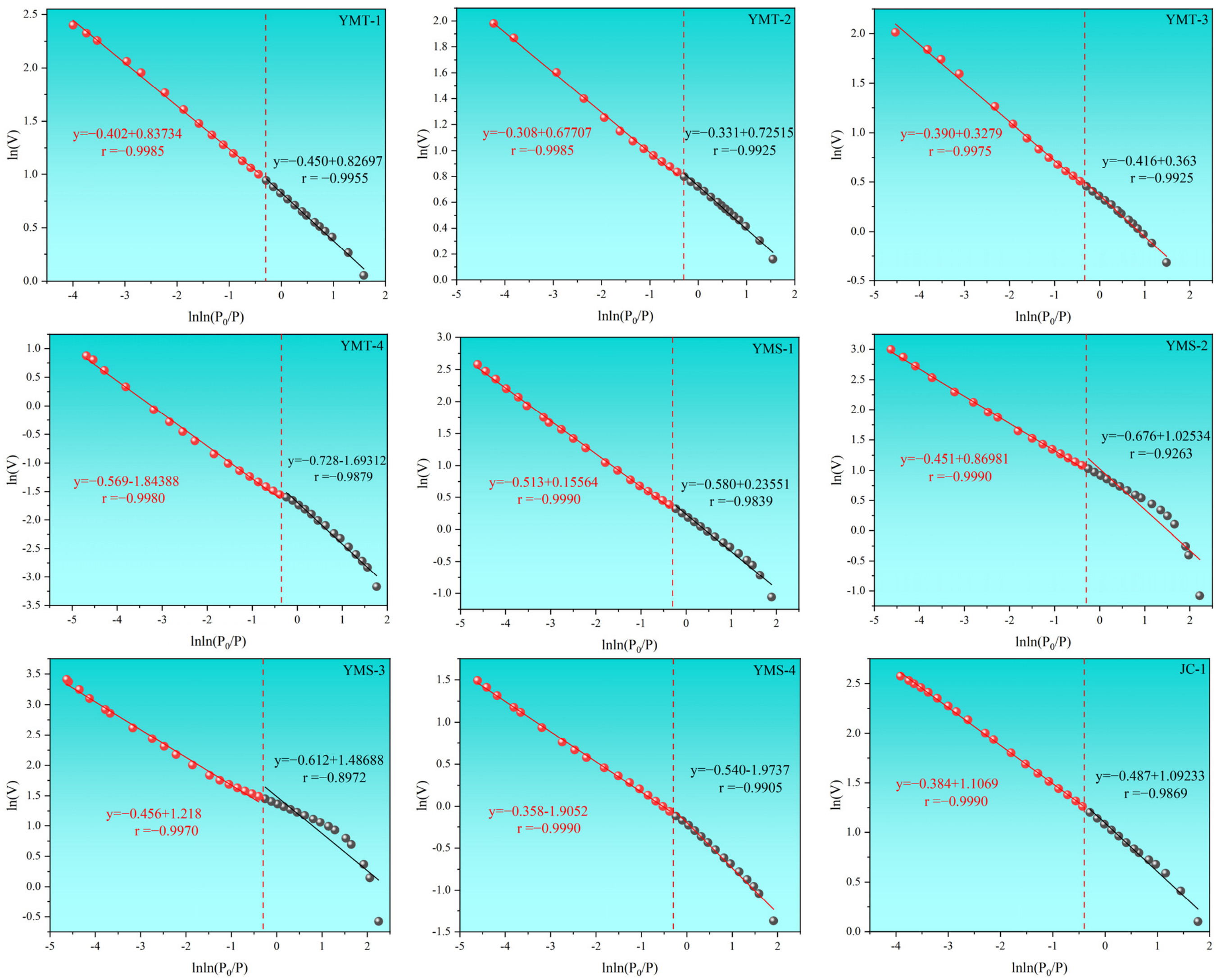

Figure 9. *Cont.*

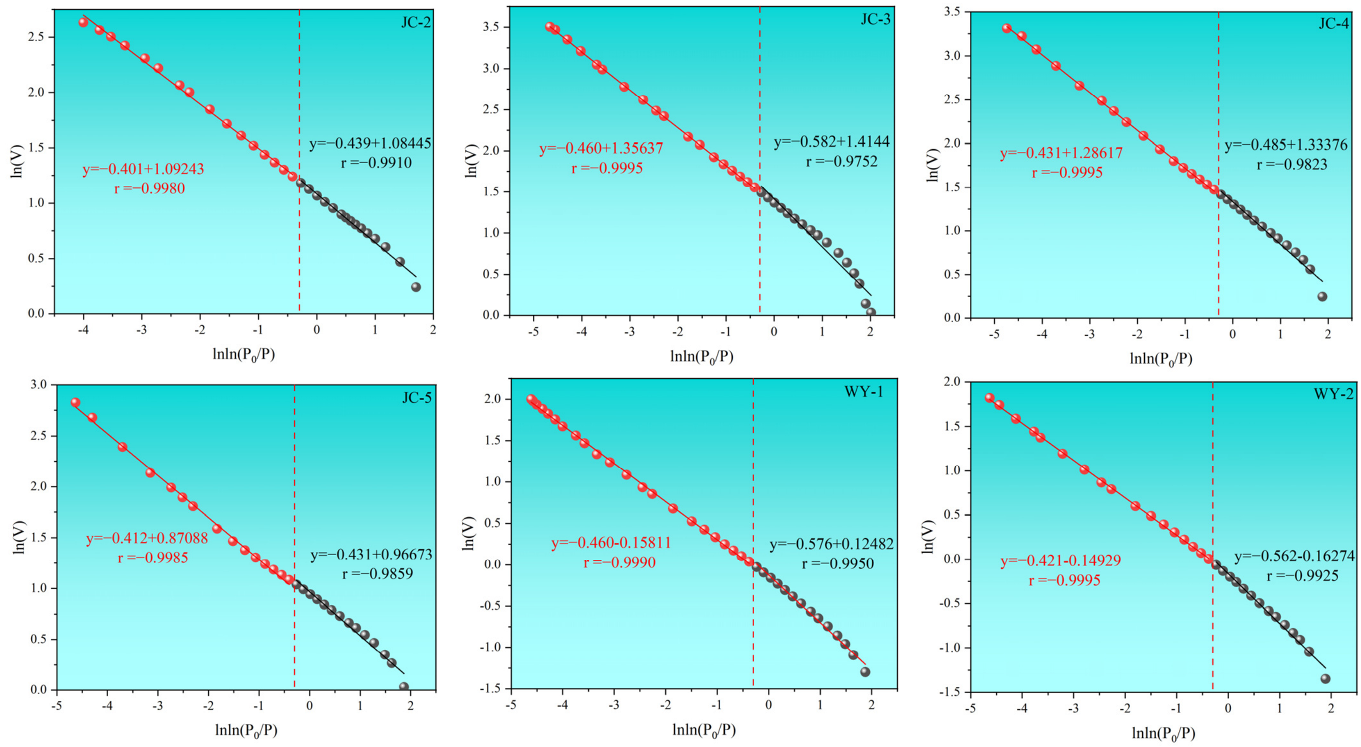

Figure 9. Fractal dimensions of samples. Left: red data points ($P/P_0 > 0.5$); Right: black data points ($P/P_0 < 0.5$).

4. Discussion

4.1. Relationships Between Mineral Composition and Pore Structure

Figures 10 and 11 illustrate the influence of antigorite, tremolite, calcite, dolomite, chlorite, and lizardite on the SSA values and PV of the Tonggou jade deposit.

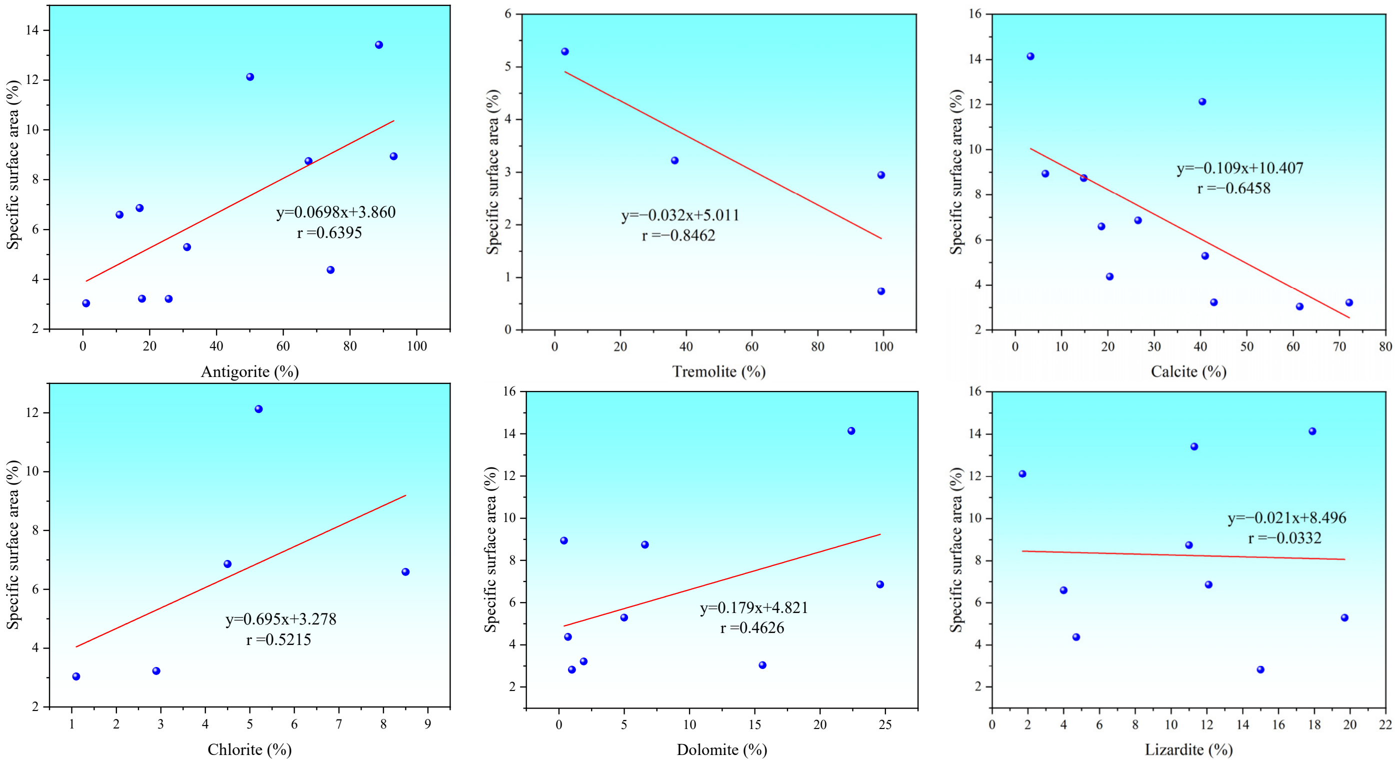

Figure 10. Correlations of SSA and mineral fraction.

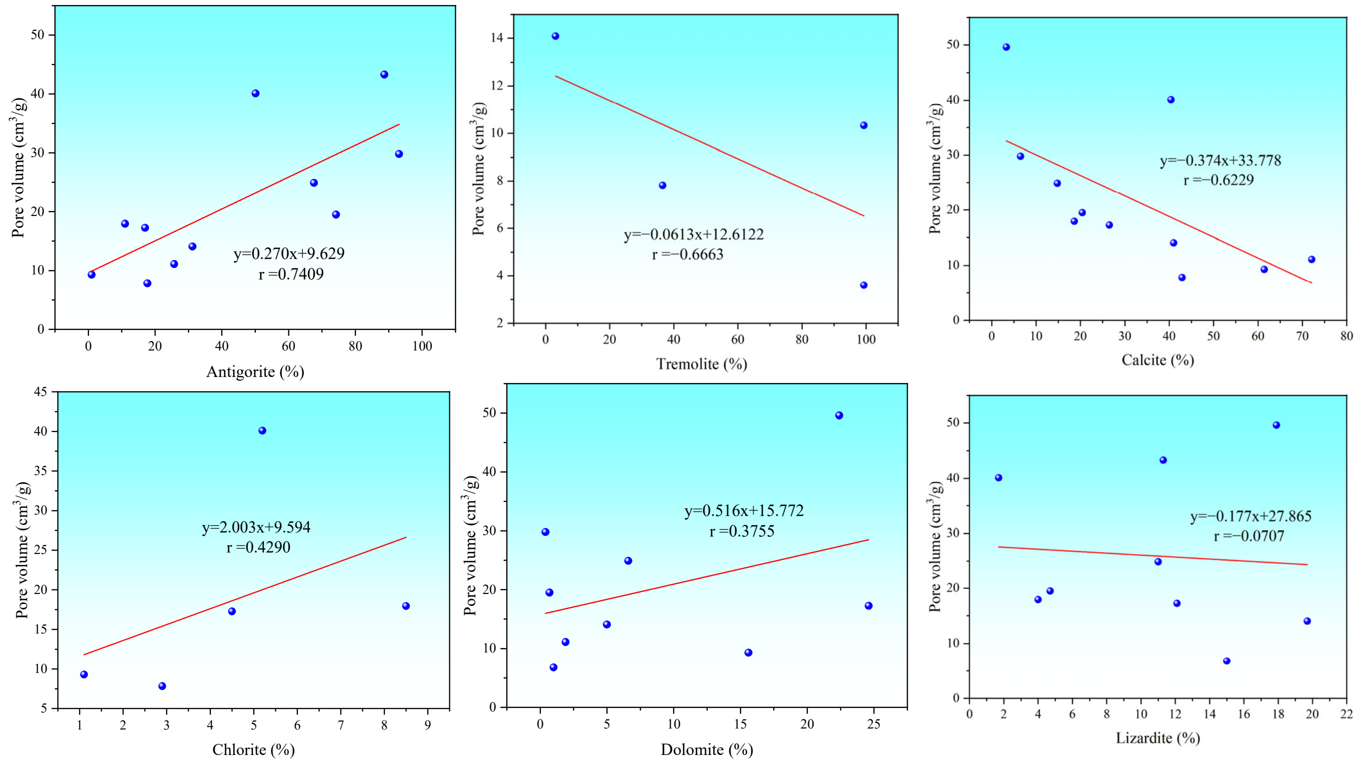

Figure 11. Correlations of PV and mineral fraction.

In the study of Tonggou jade mine, higher antigorite content correlates with increased SSA and volume of nanoscale pores. The link between antigorite and PV is higher than that between antigorite and SSA. The periodic undulations of the silica–oxygen tetrahedral layer in antigorite are positively correlated with the development of nanopores. The undulated layered structure of antigorite results in uneven stress distribution between layers, and the interlayer slip under tectonic stress facilitates the development of nanoscale tensile fractures [33–35]. The interlayer dislocation within these structures forms a connected pore network [36]. The pore SSA and PV in the Tonggou jade deposit exhibit a moderate positive link with antigorite, with a correlation coefficient of 0.6395 between antigorite and SSA, and 0.7409 between antigorite and PV. Thus, antigorite demonstrates a moderate positive relationship with both PV and SSA.

Conversely, SSA and PV decrease with increasing content of tremolite and calcite. Tremolite, belonging to the amphibole double-chain silicate minerals, features a rigid silicon–oxygen tetrahedral structure, with Ca^{2+} and Mg^{2+} closely connecting the chains. The high Si-O covalent bond ratio (>60%) and fixed bond angles within the chain result in strong resistance to deformation [37,38]. Under stress, the rigid chain structure favors lattice elastic deformation over fracture, inhibiting the formation of nanopores [39]. The correlation coefficient between tremolite and SSA is 0.8462, and between tremolite and PV is 0.6663. Therefore, tremolite minerals show a strong negative correlation with SSA and a moderate negative correlation with PV.

In the Tonggou jade deposit, the crystal lattice of calcite is closely packed, with $[CO_3]^{2-}$ triangular layers and Ca^{2+} alternating to form tightly stacked near-ideal spheres. During the formation and cultivation of jade, compressive stress induces plastic deformation of twin-crystal slip, while shear stress promotes mechanical twinning of twin crystals [40–42]. The crystal chemical characteristics of calcite actively inhibit the formation and preservation of pores. The link between calcite and SSA, PV is 0.6458 and 0.6229, respectively. Thus, calcite displays a curvilinear correlation with SSA and PV.

https://doi.org/10.3390/min16020170

Clay minerals experience dissolution and subsequent precipitation during diagenesis and jade formation, processes that occur under intense and complex tectonic movements, resulting in the formation of intricate nanoscale pores with fine structures [43]. The correlation analysis reveals that the clay mineral chlorite has a medium positive correlation with SSA (r = 0.5215). Concurrently, the amphibole mineral tremolite (a major jade-forming phase) exhibits a moderate positive correlation with PV (r = 0.4290).

The cationic ordering of dolomite leads to the formation of nano-sized isolated pores in lattice mismatch regions, but strong covalent C-O bonds restrict pore expansion. Consequently, dolomite exerts a weak promotional effect on PV and SSA area. There is no regular relationship between SSA and PV of the Tonggou jade deposit and the existence of lizardite.

4.2. The Influence of Pore Structure on Fractals

This paper analyses fractal dimensions of Tonggou jade using SSA, PV, and APS data. Outlying discrete data points were excluded. Results show correlation coefficients of 0.3372 and 0.3973 between SSA and D_{F1}, D_{F2}, respectively (Figure 12a), correlation coefficients of 0.4273 and 0.5241 between PV and D_{F1}, D_{F2} (Figure 12b), and correlation coefficients of 0.6633 and 0.9105 between APS and D_{F1}, D_{F2} (Figure 12c). As the fractal dimension grows, the relationship with the SSA, PV, and APS data decreases slowly.

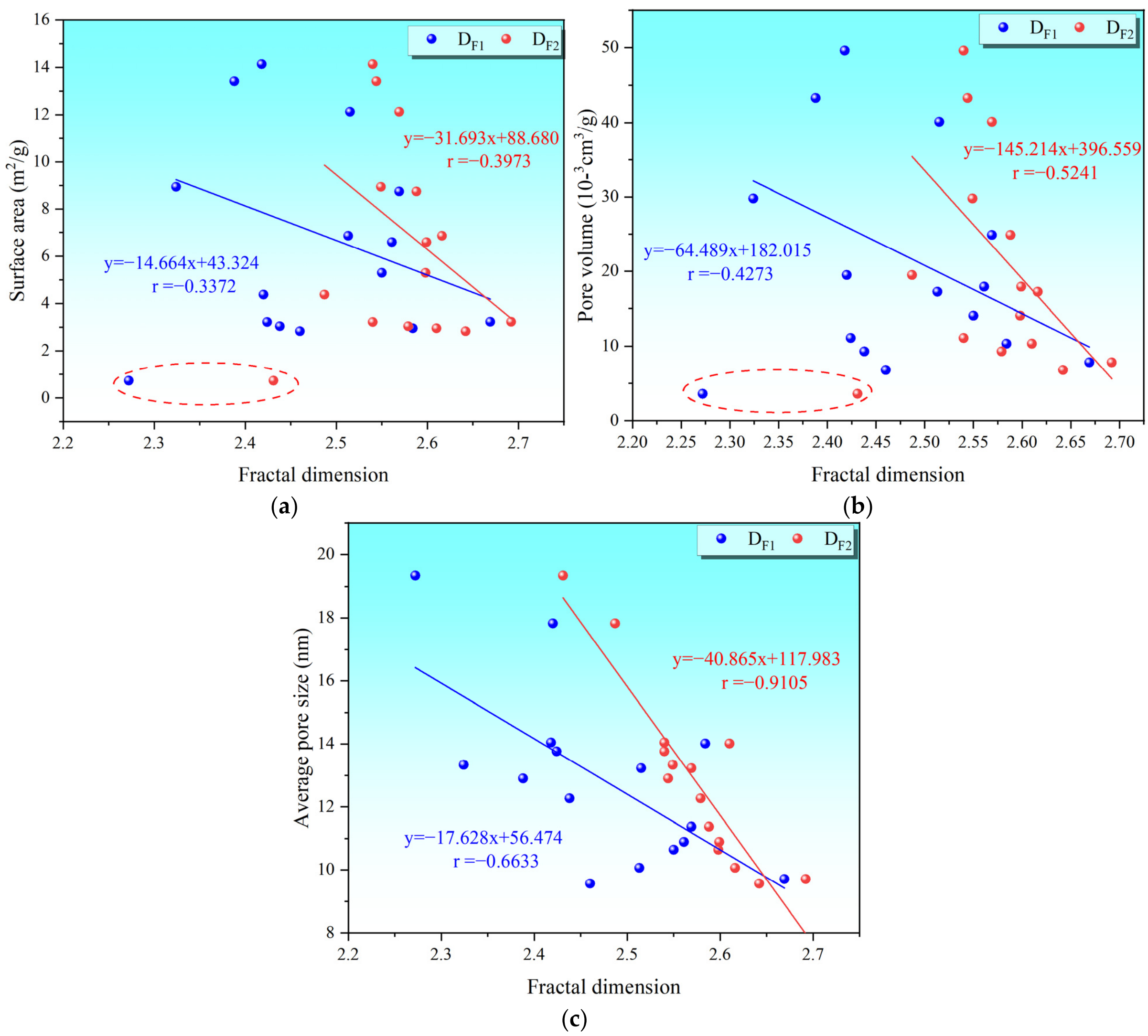

Figure 12. Relation between pore size and fractal dimension in Tonggou jade deposit: (**a**) surface area versus fractal size; (**b**) PV versus fractal size; (**c**) APS versus fractal size.

https://doi.org/10.3390/min16020170

The fractal dimensions of the Tonggou jade deposit exhibited a weak link with SSA. In the comparison between PV and fractal dimension, D_{F2} was greater than that of D_{F1}, showing a moderate negative correlation. In the comparison between APS and fractal dimension, the influence of D_{F2} was significantly stronger than that of D_{F1}, demonstrating a strong negative correlation.

The Luanchuan Group, where the Tonggou deposit is located, has undergone multiple phases of intense tectonic movements and thermal processes. The Mesoproterozoic mafic–ultramafic magmatic activity served as the primary source of serpentine protolith in the jade deposit, with the ultramafic rock body providing the material basis for subsequent serpentinization. As plate subduction intensified, fold-ductile shear zones developed in the study area, and regional metamorphic recrystallization led to tighter interlocking between mineral grains. The intrusion of Late Mesozoic granitic plutons was key to the formation of serpentine and tremolite in the Tonggou jade deposit [44–47]. Magmatic hydrothermal fluids carrying silica engage in intense metasomatic reactions with magnesium-rich carbonate minerals, leading to the serpentinization of the protolith. As hydrothermal activity evolves and superimposes in later stages, silica- and calcium-rich magmatic fluids further react with the previously formed serpentine or residual protolith, triggering the recrystallization of tremolite. In the formation of the Luanchuan jade deposit, hydrothermal magma not only acts as a material supply source but also as a reaction catalyst [48].

The broader the influence range of mineral grain pore structures and microcracks in the Tonggou jade deposit, the simpler the pore distribution within and between particles, resulting in lower values of D_{F1} and D_{F2} within the study area. Therefore, the intracontinental orogeny during the Yanshan period and the magmatic–hydrothermal activities induced by tectonic movements were the dominant factors in the formation of intragranular–intergranular pores, and microcracks in the Tonggou jade deposit, which are closely related to the negative link between fractal and the deposit's SSA, PV, and APS.

4.3. The Effect of Mineral Composition on Fractals

The formation of the Tonggou jade deposit represents a typical polyphase and multi-stage hydrothermal metasomatic and metamorphic crystallization process, wherein mineral precipitation follows an evolutionary trend from magnesium-rich to calcium–magnesium-rich assemblages. Under the influence of regional metamorphism and early-stage hydrothermal metasomatism, the magnesium-rich protolith undergoes preliminary serpentinization. Brucite is generated during this stage as a result of silica deficiency in the fluid. As the hydrothermal system evolves and superimposes in subsequent stages, the increased activity of calcium and silica in the fluid leads to the metasomatic replacement of pre-existing serpentinite or dolomitic marble, resulting in the formation of tremolite, which constitutes the primary component of nephrite. Outlying discrete data points were excluded. In the analysis of the influence of mineral classification, the outlier data points were excluded, and the composition of the jade deposit was divided into four types: siliceous minerals, clay minerals, marble minerals, and ferruginous minerals (Figure 13).

As the content of silica minerals such as tremolite, antigorite, and lizardite increases, the fractal dimension gradually rises. The correlation coefficient between D_{F1} and siliceous minerals is 0.3787, indicating a weak positive correlation. Fibrous tremolite microcrystals often form intercrystalline micropores along the C-axis, while bundled and felt-like microcrystalline aggregates grow to form abundant fractal networks [49]. With the increase in the fractal dimension of influencing factors, the microcrystalline aggregates of tremolite become more complex, and pores and microfractures become more developed. Layered silicate minerals such as serpentine typically form cleavages or fractures along their bedding planes. The wavy bedding of antigorite induces structural deformation, promoting dislocation development [50–52]. The hydroxyl structure of serpentine is prone to contraction deformation during alteration, leading to the development of pores and fractures. Hence, silica minerals such as tremolite and serpentine exhibit a positive correlation with the fractal dimension. However, since tremolite is prone to plastic deformation under high-temperature alteration, which heals microfractures, and serpentine is cemented and filled by later carbonate minerals in intergranular pores, the overall correlation between silica minerals and the fractal dimension is weakly positive [53,54].

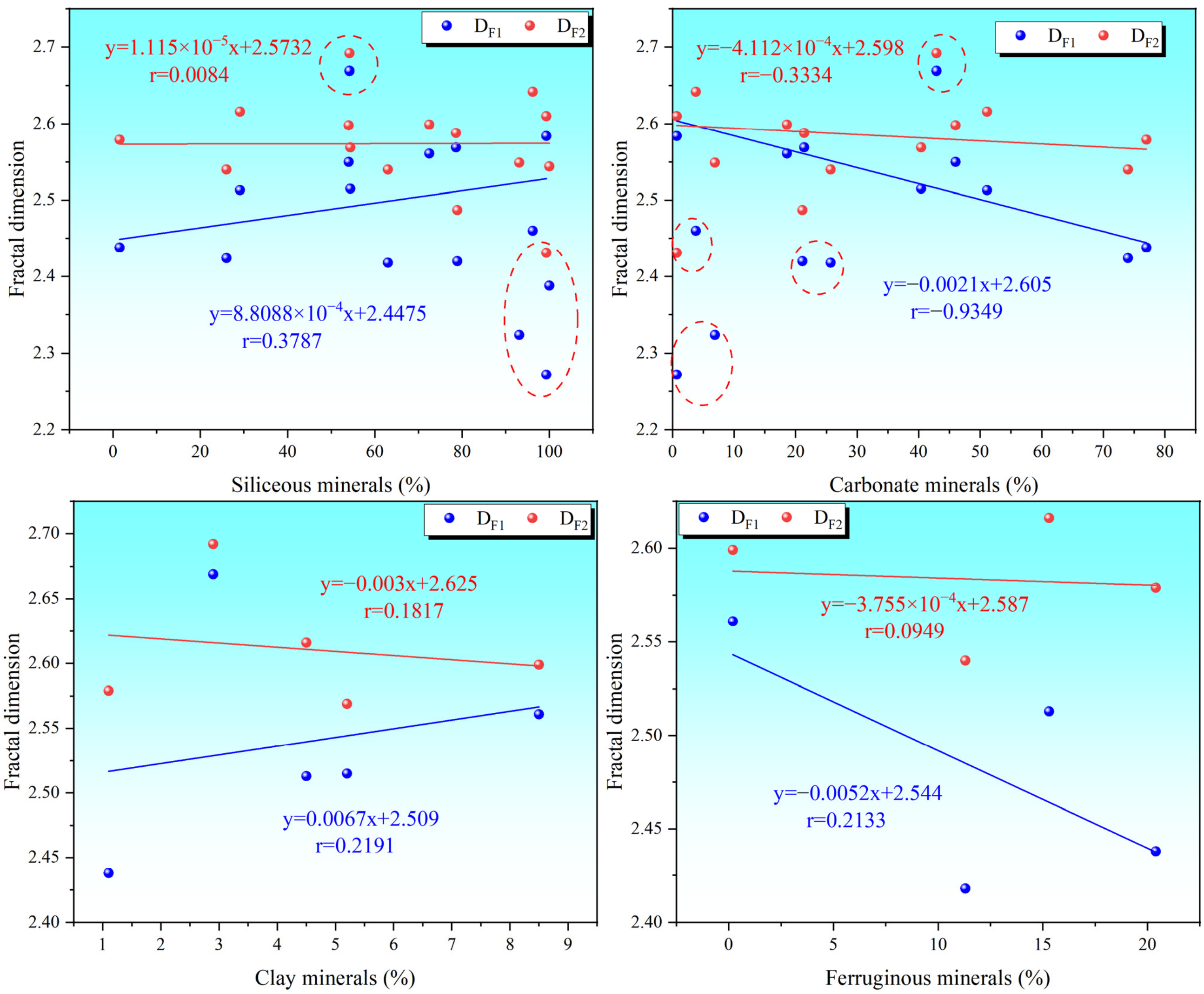

Figure 13. Variation diagram of mineral components with fractal dimensions.

The correlation coefficient between carbonate minerals such as calcite and dolomite in the Tonggou jade deposit and the fractal dimension D_{F1} is 0.9349, indicating a strong negative link between carbonate content and fractal dimension. Calcite has perfect rhombohedral cleavage on {1014}, and under stress, cleavage planes slide to form relatively regular pores and fractures [55,56]. Dolomite is prone to recrystallization under high temperatures, promoting healing and development of pores and fractures. Therefore, as the content of carbonate minerals in the Tonggou jade deposit increases, the pore system becomes simpler, and the fractal dimension gradually decreases.

With the increase in clay minerals and iron-bearing minerals, the fractal dimension shows no significant change. This is because fibrous chlorite minerals can both increase pore space and, under certain conditions, block the development of pores and fractures [57]. Their complex growth variations make their impact on fractal dimension data less noticeable. Due to low content, iron-bearing minerals do not exhibit a discernible pattern in the fractal dimension data of the Tonggou jade deposit.

In western Henan, Luanchuan, regional tectonic compression and folding provided the necessary conduits for fluid migration. The multi-stage evolution and superposition of magnesium-rich to calcium–magnesium-rich hydrothermal fluids resulted in the characteristic paragenesis of "serpentine–nephrite–marble" observed in Yiyuan jade.

5. Conclusions

This paper examines the pore characteristics and fractal dimensions of the Tonggou nephrite deposit, utilizing experimental techniques such as XRD, SEM, and LT-N_2GA, FHH model for data analysis. The following conclusions have been drawn:

1. The development of the pore network (including intraparticle pores, interparticle pores, and microfractures) in the Tonggou nephrite deposit affects the arrangement and combination of jade mineral particles, which in turn influences the quality evaluation and value potential assessment of the processed Yiyuan jade. The study area is characterized by a high content of silica minerals and a low content of clay minerals. The curve analysis of the Tonggou nephrite deposit exhibits Type IV characteristics, consistent with the H_2 and H_3 types in the IUPAC classification. The D_{F2} data are higher than the D_{F1} data, but no clear regular correlation exists between them.
2. In the Tonggou nephrite deposit, antigorite and clay mineral chlorite show positive correlations with SSA and PV, while tremolite exhibits a strong negative correlation with SSA and a moderate negative correlation with PV. Calcite demonstrates moderate negative correlations with them. Dolomite has a relatively weak promoting effect on PV and SSA. The presence of lizardite shows no systematic relationship with them.
3. The fractal dimension of the Tonggou nephrite deposit exhibits a weak correlation with SSA. In the comparison between PV and fractal dimension, D_{F2} is greater than D_{F1}, showing a moderate negative correlation. In the comparison between APS and fractal dimension, D_{F2} is significantly higher than D_{F1}, displaying a strong negative correlation.
4. As the content of siliceous minerals increases, the fractal dimension also gradually rises, indicating a weak positive correlation. Conversely, with the rise in carbonate mineral content, the pore system becomes simpler, and the fractal dimension decreases. The complex growth and variation in clay minerals result in a less pronounced impact on the fractal dimension data.

Author Contributions: Conceptualization, X.W. and Q.M.; methodology, X.W. and W.L.; software, X.W. and J.S.; validation, X.W., L.Z. and W.W.; formal analysis, X.W. and W.L.; investigation X.W. and W.L.; resources, data curation, X.W., L.Z. and W.W.; writing—original draft preparation, X.W.; writing—review and editing, W.L., X.W. and W.W.; visualization, X.W. and W.L.; supervision, W.L., X.W. and W.W.; project administration, X.W., Q.M. and J.S. All authors have read and agreed to the published version of the manuscript.

Funding: The research was supported by the National Natural Science Foundation of China (No. 42002031) and the Henan Provincial Science and Technology Program of the Market Supervision Administration Bureau (No. 2023sj38).

Data Availability Statement: All relevant data are placed in the body of the article.

Conflicts of Interest: The authors declare no conflicts of interest.

References

1. Chen, K.Q.; Chen, Z.Y. Study on compositions and physical features of Hetian jade. *Acta Petrol. Mineral.* **2002**, *21*, 34–40.
2. Zhang, C.; Yu, X.Y.; Jiang, T.L. Mineral association and graphite inclusions in nephrite jade from Liaoning, northeast of China: Implications for metamorphic conditions and ore genesis. *Geosci. Front.* **2019**, *10*, 425–437. [CrossRef]
3. Liu, Y.; Deng, J.; Shi, G.H.; Yu, T.F.; Zhang, G. Geochemistry and petrology of nephrite from Alams, NW China. *Asian Earth Sci.* **2011**, *42*, 440–451. [CrossRef]
4. Liu, Y.; Zhang, R.; Zhang, Z.; Shi, G.H.; Zhang, Q.; Anuduwayiti, M.; Liu, J. Mineral inclusions and SHRIMP U–Pb dating of zircons from the Alamas nephrite and granodiorite: Implications for the genesis of a magnesian skarn deposit. *Lithos* **2015**, *212–215*, 128–144. [CrossRef]
5. Harlow, G.E.; Sorenson, S.S. Jade (nephrite and jadeitite) and serpentinite: Metasomatic connections. *Int. Geol. Rev.* **2005**, *47*, 114–128. [CrossRef]
6. Liu, Y.; Deng, J.; Shi, G.H.; Sun, X.; Yang, L. Geochemistry and petrogenenesis placer nephrite from Hetian, Xinjiang Northwest China. *Ore Geol. Rev.* **2011**, *41*, 122–132. [CrossRef]
7. Yui, T.F.; Kwon, S.T. Origin of a dolomite-related jade deposit at Chuncheon, Korea. *Econ. Geol.* **2002**, *l97*, 593–601. [CrossRef]
8. Hockley, J.J.; Birch, W.D.; Worner, H.K. Anephrite deposit in the great serpentinebelt of New South Wales. *J. Geol. Soc. Aust.* **1978**, *25*, 249–254. [CrossRef]
9. Harlow, G.E.; Sorensen, S.S.; Sisson, V.B.; Shi, G. Chapter 10: The Geology of Jade Deposits. In *The Geology of Gem Deposits*, 2nd ed.; Groat, L.A., Ed.; Short Course Handbook Series; Mineralogical Association of Canada: Sudbury, ON, Canada, 2014; Volume 44, pp. 305–374.
10. Yui, T.F.; Usuki, T.; Chen, C.Y.; Ishida, A.; Sano, Y.; Suga, K.; Iizuka, Y.; Chen, C.T. Dating thin zircon rims by NanoSIMS: The Fengtien nephrite (Taiwan) is the youngest jade on Earth. *Int. Geol. Rev.* **2014**, *56*, 1932–1944. [CrossRef]
11. Bebout, G.E.; Penniston-Dorland, S.C. Fluid and mass transfer at subduction interfaces-the field metamorphic record. *Lithos* **2016**, *240*, 228–258. [CrossRef]
12. Wang, G.Q.; Li, X.M.; Yu, J.Y.; Tang, Z.; Zhu, T.; Pan, F.; Zhang, Y.; Bu, T. LA-ICP-MS zircon U-Pb dating of syenite from Yushigou in Northern Qilian Mountain. *Geol. Bull. China* **2018**, *37*, 532–537.
13. Yin, Z.; Jiang, C.; Santosh, M.; Chen, Y.M.; Bao, Y.; Chen, Q.L. Nephrite Jade from Guangxi Province, China. *Gems Gemol.* **2014**, *50*, 228–235. [CrossRef]
14. Gao, K.; Shi, G.H.; Wang, M.L.; Xie, G.; Wang, J.; Zhang, X.C.; Fang, T.; Lei, W.Y.; Liu, Y. The Tashisayi nephrite deposit from South Altyn Tagh, Xinjiang, Northwest China. *Geosci. Front.* **2019**, *10*, 1597–1612. [CrossRef]
15. Ling, X.X.; Schmädicke, E.; Qiu, L.-L.; Gose, J.; Wu, R.H.; Wang, S.Q.; Liu, Y.; Tang, G.Q.; Li, X.H. Age determination of nephrite by in-situ SIMS U–Pb dating syngenetic titanite: A case study of the nephrite deposit from Luanchuan, Henan, China. *Lithos* **2015**, *220–223*, 289–299.
16. Huber, M.; Stępniewska, K. Application of the Fractal Dimension Calculation Technique to Determine the Shape of Selected Monchepluton Intrusion Crystals (NE Fennoscandia). *Minerals* **2021**, *11*, 1140. [CrossRef]
17. Zhao, F.; Sun, Q.; Zhang, W. Fractal analysis of pore structure of granite after variable thermal cycles. *Environ. Earth Sci.* **2019**, *78*, 677. [CrossRef]
18. Li, Y.; Yang, J.S.; Dilek, Y.; Zhang, J.; Pei, X.Z.; Chen, S.Y.; Xu, X.Z.; Li, J.Y. Crustal architecture ofthe Shangdan suture zone in the early Paleozoic Qinling orogenic belt, China: Record of subduction initiation and backarc basin development. *Gondwana Res.* **2015**, *27*, 733–744. [CrossRef]
19. Bader, T.; Franz, L.; Ratschbacher, L.; De Captitani, C.; Webb, A.A.G.; Yang, Z.; Pfänder, J.A.; Hofmann, M.; Linnemann, U. The heart of China revisited: II Early Paleozoic (ultra) high-pressure and (ultra) high-temperature metamorphic Qinling orogenic collage. *Tectonics* **2013**, *32*, 922–947. [CrossRef]
20. Su, W.; Liu, J.B.; Chen, N.S.; Guo, S.; Ba, J.; Zhang, L.; Liu, X.; Shi, Y.X. Geochronology and tectonic background ofmagmatic and metamorphic events in the East Qinling–Dabie Mountains. *Acta Petrol. Sin.* **2013**, *29*, 1573–1593.
21. Scott, J.M.; Smith, S.A.; Tarling, M.S.; le Roux, P.J.; Harris, C.; Hoffmann, J.E.; Scherzer, S.; Tulley, C.J. Element and Sr–O isotope redistribution across a plate boundary-scale crustal serpentinite m′ elange shear zone, and implications for the slab-mantleinterface. *Earth Planet. Sci. Lett.* **2019**, *522*, 198–209. [CrossRef]
22. Angiboust, S.; Wolf, S.; Burov, E.; Agard, P.; Yamato, P. Effect of fluid circulation on subduction interface tectonic processes: Insights from thermo-mechanical numerical modelling. *Earth Planet. Sci. Lett.* **2012**, *357–358*, 238–248. [CrossRef]
23. Mao, J.W.; Pirajno, F.; Xiang, J.F.; Gao, J.J.; Ye, H.S.; Li, Y.F.; Guo, B.J. Mesozoic molybdenum deposits in the East Qinling-Dabie Orogenic belt: Characteristics and tectonic settings. *Ore Geol. Rev.* **2011**, *43*, 264–293. [CrossRef]
24. Li, D.; Zhang, S.T.; Yan, C.H.; Wang, G.W.; Song, Y.W.; Ma, Z.B.; Han, J.W. Late Mesozoic time constraints on tectonic changes of the Luanchuan Mo belt East Qinling orogen Central China. *J. Geodynam.* **2012**, *61*, 94–104. [CrossRef]
25. Yang, Y.; Chen, Y.J.; Zhang, J.; Zhang, C. Ore geology, fluid inclusions and fourstage hydrothermal mineralization of the Shangfanggou giant Mo–Fe deposit in Eastern Qinling, central China. *Ore Geol. Rev.* **2013**, *55*, 146–161. [CrossRef]

26. Wood, D.A. Techniques used to calculate shale fractal dimensions involve uncertainties and imprecisions that require more careful consideration. *Adv. Geo-Energy Res.* **2021**, *5*, 153–165. [CrossRef]
27. Lai, Y.; Zhao, K.; He, Z.; Yu, X.; Yan, Y.; Li, Q.; Shao, H.; Zhang, X.; Zhou, Y. Fractal characteristics of rocks and mesoscopic fractures at different loading rates. *Geomech. Energy Environ.* **2023**, *33*, 100431. [CrossRef]
28. Angiboust, S.; Pettke, T.; De Hoog, J.C.M.; Caron, B.; Oncken, O. Channelized fluid flow eclogite-facies metasomatism along the subduction shear zone. *J. Petrol.* **2014**, *55*, 883–916. [CrossRef]
29. Angiboust, S.; Yamato, P.; Hertgen, S.; Hyppolito, T.; Bebout, G.E.; Morales, L. Fluid pathways high-P metasomatism in a subducted continental slice (Mt. Emilius klippe, W. Alps). *J. Metamorph. Geol.* **2017**, *35*, 471–492. [CrossRef]
30. Jafarian, Y.; Javdanian, H. Small-strain dynamic properties of siliceous-carbonate sand under stress anisotropy. *Soil Dyn. Earthq. Eng.* **2020**, *131*, 106045. [CrossRef]
31. Zheru, Z.; Huahi, M.; Cheng, Q. Fractal Geometry of Element Distribution on Mineral Surfaces. *Math. Geol.* **2001**, *33*, 217–228. [CrossRef]
32. Zhang, J.Z.; Tang, Y.J.; He, D.X.; Sun, P.; Zou, X.Y. Full-scale Nanopore System and Fractal Characteristics of Clay-rich Lacustrine Shale Combining FE-SEM, Nano-CT, Gas Adsorption and Mercury Intrusion Porosimetry. *Appl. Clay Sci.* **2020**, *196*, 105758. [CrossRef]
33. Cannaò, E.; Scambelluri, M.; Bebout, G.E.; Agostini, S.; Pettke, T.; Godard, M.; Crispini, L. Ophicarbonate evolution from seafloor to subduction and implications for deep-Earth C cycling. *Chem. Geol.* **2020**, *546*, 119626. [CrossRef]
34. Padr'on-Navarta, J.A.; Tommasi, A.; Garrido, C.J.; López Sánchez-Vizcaíno, V. Plastic deformation and development of antigorite crystal preferred orientation in high-pressure serpentinites. *Earth Planet. Sci. Lett.* **2012**, *349–350*, 75–86. [CrossRef]
35. Deschamps, F.; Godard, M.; Guillot, S.; Hattori, K. Geochemistry of subduction zone serpentinites: A review. *Lithos* **2013**, *178*, 96–127. [CrossRef]
36. Llanes Castro, A.I.; Furnes, H.; Cruz Gámez, E.M.; Rodriguez, M.P.; Cruz, O.L. Petrogenesis of plagiogranite and associated diorites and mafic rocks in the Habana–Matanzas ophiolites northwestern half of central Cuba. *J. Geol. Soc. Lond.* **2018**, *176*, 992–1006. [CrossRef]
37. Hawthorne, F.C.; Oberti, R.; Harlow, G.E.; Maresch, W.V.; Martin, R.F.; Schumacher, J.C.; Welch, M.D. Ima report: Nomenclature of the amphibole supergroup. *Am. Mineral.* **2012**, *97*, 2031–2048. [CrossRef]
38. Han, J.S.; Yao, J.M.; Chen, H.Y.; Deng, X.H.; Ding, J.Y. Fluid inclusion and stable isotope study of the Shagou Ag–Pb–Zn deposit, Luoning, Henan province, China: Implications for the genesis of an orogenic lode Ag–Pb–Zn system. *Ore Geol. Rev.* **2014**, *62*, 199–210. [CrossRef]
39. Li, D. Tectono-Magmatism Evolution of Mo Polymetallic Ore, Metallogenesis and Prediction for Deep Ore Prospecting in Luanchuan Ore Belt. Ph.D. Thesis, China University of Geosciences (Beijing), Beijing, China, 2014; pp. 1–120.
40. Duan, S.G.; Xue, C.J.; Feng, Q.W.; Gao, B.Y.; Liu, G.Y.; Yan, C.H.; Song, Y.W. Carbon and oxygen isotope compositions of gangue carbonates in Pb–Zn ore deposits in Luanchuan District, Southwest Henan Province. *Geoscience* **2010**, *24*, 767–775.
41. Bouilhol, P.; Burg, J.P.; Bodinier, J.L.; Schmidt, M.W.; Bernasconi, S.M.; Dawood, H. Gem olivine and calcite mineralization precipitated from subduction-derived fluids in the kohistan arc-mantle (Pakistan). *Can. Mineral.* **2012**, *50*, 1291–1304. [CrossRef]
42. Molina, J.F.; Poli, S. Carbonate stability and fluid composition in subducted oceanic crust: An experimental study on H_2O-CO_2-bearing basalts. *Earth Planet. Sci. Lett.* **2000**, *176*, 295–310. [CrossRef]
43. Padón-Navarta, J.A.; Sánchez-Vizcaí, V.L.; Garrido, C.J.; Gómez-Pugnaire, M.T. Metamorphic record of high-pressure dehydration of antigorite serpentinite to chlorite harzburgite in a subduction setting (Cerro del Almirez Nevado-Fil' abride complex Southern Spain). *J. Petrol.* **2011**, *52*, 2047–2078. [CrossRef]
44. Wang, X.L.; Jiang, S.Y.; Dai, B.Z.; Griffin, W.L.; Dai, M.N.; Yang, Y.H. Age, geochemistry and tectonic setting of the Neoproterozoic (ca 830 Ma) gabbros on the southern margin of the North China Craton. *Precambrian Res.* **2011**, *190*, 35–47. [CrossRef]
45. Dong, Y.P.; Zhang, G.W.; Neubauer, F.; Liu, X.M.; Genser, J.; Hauzenberger, C. Tectonic evolution of the Qinling orogen China: Review synthesis. *J. Asian Earth Sci.* **2011**, *41*, 213–237. [CrossRef]
46. Li, N.; Chen, Y.J.; Santosh, M.; Pirajno, F. Compositional polarity of Triassic granitoids in the Qinling Orogen, China: Implication for termination of the northernmost paleo-Tethys. *Gondwana Res.* **2015**, *27*, 244–257. [CrossRef]
47. Angiboust, S.; Muñoz-Montecinos, J.; Cambeses, A.; Raimondo, T.; Deldicque, D.; Garcia-Casco, A. Jolts in the Jade factory: A route for subduction fluids and their implications for mantle wedge seismicity. *Earth-Sci. Rev.* **2021**, *220*, 103720. [CrossRef]
48. Yin, J.N. Petrology and Deposit Research on Nephrite and Serpentine of Luan Chuan, Henan Province. Master's Thesis, China University of Geosciences (Beijing), Beijing, China, 2006. (In Chinese with English abstract).
49. Padrón-Navarta, J.A.; Sánchez-Vizcaíno, V.L.; Hermann, J.; Connolly, J.A.D.; Garrido, C.J.; Gómez-Pugnaire, M.T.; Marchesi, C. Tschermak's substitution in antigorite and consequences for phase relations and water liberation in high-grade serpentinites. *Lithos* **2013**, *178*, 186–196. [CrossRef]
50. Evans, B.W. The serpentinite multisystem revisited: Chrysotile is metastable. *Int. Geol. Rev.* **2004**, *46*, 479–506. [CrossRef]
51. Hacker, B.R. H_2O subduction beyond arcs. *Geochem. Geophys. Geosystems* **2008**, *9*, Q03001. [CrossRef]

52. Deschamps, F.; Guillot, S.; Godard, M.; Chauvel, C.; Andreani, M.; Hattori, K. In situ characterization of serpentinites from forearc mantle wedges: Timing of serpentinization and behavior of fluid-mobile elements in subduction zones. *Chem. Geol.* **2010**, *269*, 262–277. [CrossRef]
53. Ren, W.D.; Yang, F.; Bagas, L.; Zhang, C.; Chi, N.J.; Zhang, X.H. In-situ molybdenite and rutile geochemistry of the Nannihu porphyry Mo-W deposit, East Qinling, China: A perspective on ore-forming processes. *Ore Geol. Rev.* **2023**, *164*, 105823. [CrossRef]
54. Yang, F.; Wen, Y.M.; Jepson, G.; Santosh, M.; Wu, L.; Shen, X.M.; Ali, H. Prolonged exhumation and preservation of the Yuku molybdenum ore field, East Qinling, China: Constraints from medium- to low-temperature thermochronology. *Ore Geol. Rev.* **2024**, *167*, 105973. [CrossRef]
55. Munoz-Montecinos, J.; Angiboust, S.; Garcia-Casco, A.; Glodny, J.; Bebout, G. Episodic hydrofracturing and large-scale flushing along deep subduction interfaces:Implications for fluid transfer and carbon recycling (Zagros Orogen, southeastern Iran). *Chem. Geol.* **2021**, *571*, 120173. [CrossRef]
56. Plümper, O.; John, T.; Podladchikov, Y.Y.; Vrijmoed, J.C.; Scambelluri, M. Fluid escape from subduction zones controlled by channel-forming reactive porosity. *Nat. Geosci.* **2017**, *10*, 150–156. [CrossRef]
57. Gao, Q.-F.; Jrad, M.; Hattab, M.; Fleureau, J.-M.; Ighil Ameur, L. Pore Morphology, Porosity, and Pore Size Distribution in Kaolinitic Remolded Clays under Triaxial Loading. *Int. J. Geomech.* **2020**, *20*, 04020057. [CrossRef]

https://doi.org/10.3390/min16020170